ASME Journal of Manufacturing Science and Engineering
Online journal at:
https://asmedigitalcollection.asme.org/manufacturingscience

Zoe Alexander
Mem. ASME
George W. Woodruff School of Mechanical Engineering and School of Computational Science and Engineering,
Georgia Institute of Technology,
Atlanta, GA 30332
e-mail: zklesmith3@gatech.edu

Thomas Feldhausen
Mem. ASME
Manufacturing Sciences Division,
Oak Ridge National Laboratory,
Oak Ridge, TN 37830
e-mail: feldhausenta@ornl.gov

Kyle Saleeby
Mem. ASME
Manufacturing Sciences Division,
Oak Ridge National Laboratory,
Oak Ridge, TN 37830
e-mail: saleebyks@ornl.gov

Thomas Kurfess
Professor
Fellow ASME
George W. Woodruff School of Mechanical Engineering,
Georgia Institute of Technology,
Atlanta, GA 30332
e-mail: kurfess@gatech.edu

Katherine Fu
Associate Professor
Mem. ASME
Department of Mechanical Engineering,
University of Wisconsin-Madison,
Madison, WI 53706
e-mail: kate.fu@wisc.edu

Christopher Saldaña[1]
Associate Professor
Mem. ASME
George W. Woodruff School of Mechanical Engineering, Georgia Institute of Technology,
Atlanta, GA 30332
e-mail: christopher.saldana@me.gatech.edu

Data-Driven Approaches for Bead Geometry Prediction Via Melt Pool Monitoring

In the realm of additive manufacturing, the selection of process parameters to avoid over and under deposition entails a time-consuming and resource-intensive trial-and-error approach. Given the distinct characteristics of each part geometry, there is a pressing need for advancing real-time process monitoring and control to ensure consistent and reliable part dimensional accuracy. This research shows that support vector regression (SVR) and convolutional neural network (CNN) models offer a promising solution for real-time process control due to the models' abilities to recognize complex, non-linear patterns with high accuracy. A novel experiment was designed to compare the performance of SVR and CNN models to indirectly detect bead height from a coaxial image of a melt pool from a single-layer, single bead build. The study showed that both SVR and CNN models trained on melt pool data collected from a coaxial optical camera can accurately predict the bead height with a mean absolute percentage error of 3.67% and 3.68%, respectively. [DOI: 10.1115/1.4062800]

Keywords: additive manufacturing, advanced materials and processing, computer-integrated manufacturing, sensing, monitoring, and diagnostics

1 Introduction

Additive manufacturing (AM) refers to a manufacturing process that utilizes 3D models to create parts by joining materials together layer-by-layer [1]. Directed energy deposition (DED) is a specialized form of metal AM process where a laser and metal powder intersect to generate a molten metal pool, known as a melt pool, on a substrate. This pool cools and solidifies to form a continuous metal track. This process is repeated layer-by-layer to create a final part. DED stands out among other metal (AM) processes due to its unique ability to manufacture sizable workpieces, contract near net shapes, and effectively repair existing parts and castings [2–4]. In addition, DED can be utilized for the

[1]Corresponding author.

Manuscript received January 18, 2023; final manuscript received June 15, 2023; published online July 20, 2023. Assoc. Editor: Arif S. Malik.

development of advanced materials such as graded materials [5], which enables the combination of metal powders to be used in a single part at different locations for optimized design. Therefore, AM technologies introduce substantial innovation to the field of manufacturing. Compared to traditional subtractive manufacturing, AM allows for unrivaled flexible design [6]. Regardless of the aforementioned benefits of DED, the industry-wide adoption of this process depends upon improvements in process monitoring and control due to unreliable part quality. In particular, subtle changes in the operating parameters can cause poor part quality due to the high sensitivity of the laser [7]. By utilizing a feedback-based approach, the laser can be dynamically adjusted to minimize process fluctuations without needing to refer to a particular, previously tested geometry and deposition history. Non-contact instruments have gained widespread popularity in similar applications due to their capability to gather information at a safe distance from the heat generated during the deposition process. Sensor damage can easily occur due to the high temperatures from the laser which cause high melting temperatures, high power laser light reflections, and spatter. When taking into account cost and ease of integration, beam-coaxial melt pool monitoring with a visible-light camera remains a practical and cost-effective solution. This is because many deposition heads for DED are equipped with a port for including a monitoring camera into the optical chain [8]. As a result, this work aims to create a vision-based setup that can locate anomalies in bead height indirectly via the energy content of the melt pool, allowing for the prediction and correction of potential deviations from the planned deposition result. In order to anticipate variations in track geometry, an investigation was conducted into the application of machine learning (ML) algorithms, specifically support vector regression (SVR) and convolutional neural networks (CNNs) for regression. Furthermore, a data collection and labeling pipeline was established to streamline the data preparation process. The developed models were then assessed for their feasibility to be integrated onto an edge device, facilitating closed-loop or feed-forward control of the machine.

2 Background

A literature review was conducted to understand the current and previous solutions regarding DED bead geometry monitoring and control. This section discusses the literature review finding and categorizes them by monitoring method.

2.1 Coaxial Optical Monitoring Systems. The study described in this paper utilized a coaxial optical camera for data acquisition. Coaxial monitoring systems offer a cost-effective and convenient solution for monitoring the melt pool, as they can be easily integrated into the existing architecture of laser-based AM machines. Moreover, the camera sensors are positioned at a safe distance from laser reflections and high process temperatures. This not only ensures the protection of the monitoring equipment but also enables contact-less and precise measurements for real-time control without interrupting the process or waiting for the deposition to cool. In the specific configuration used, the camera captures the back reflection of the melt pool using a mirror in the coaxial setup. Alternatively, off-axis camera positioning can be combined with a dichroitic mirror to align the image sensors with the reflected melt pool image. Coaxial monitoring configurations are primarily employed for direct measurements of melt pool diameter, plume behavior, and thermal conditions.

2.2 Additional Vision-Based Monitoring Systems. As a substitute to coaxial optical monitoring systems, Song and Mazumder [9] propose an in-axis pyrometer for the indirect measurement of layer height. Song and Mazumder suggested this approach because it was observed that when the laser power was out of focus, the energy density was lower, and, as a result, the pyrometers temperature reading was reduced. Among the papers reviewed, Ref. [9] is one of the few that suggested the utilization of indirect measurement through melt pool monitoring. If the camera fails to capture an overhead image of the melt pool, it was categorized as off-axial. Frequently, cameras were positioned at 45 deg from the build surface to measure melt pool plume, powder capture efficiency [10], and spatter [11]. To measure layer height, cameras were positioned either "in-line" or 90 deg from the laser axis. Jiao et al. also suggested the use of off-axial cameras for indirect measurement of weld penetration depth [12]. Jiao et al. were able to show that with only a top view of the weld bead, deep learning could be used to accurately predict weld penetration depth. In addition, camera triangulation offered an alternative approach to melt pool monitoring. This technique involved the positioning of three cameras to capture a comprehensive three-dimensional perspective of the target process. For instance, Donadello et al. employed triangulation to estimate parameters such as powder catchment efficiency and layer height [13]. Although optical triangulation is considered a useful tool for analyzing processes, it can be too interfering to be practical for application in a production environment due to the need for multiple cameras and increased calibration time. Lastly, a triangulation setup can limit machine capabilities due to the size of the monitoring setup.

2.3 Alternative Monitoring Systems. Upon reviewing the existing literature, vision-based methods were by far the most common monitoring systems for melt pool control and layer geometry prediction; however, vision-alternative methods for melt pool monitoring include multi-modal sensing, in-machine probing, and 3D scanning. Multi-modal sensing is a method to combine image sensing with other types of sensors. For example, Jamnikar et al. used multi-modal sensing to create a ML model to establish a mapping between melt pool image and temperature to geometric shape and micro-structural properties [14]. Moreover, this multi-modal network required inputs from both images and temperature measurements to train the algorithm. This method proved successful for in situ, real-time quality control; however, the setup required for multi-modal sensing can be time intensive and potentially invasive. Another alternative to controlling layer height was physically measuring it. Many DED machines are equipped with in-machine probes which can be programed to measure the part in between layers. For example, in a study conducted by Kono et al., it was shown that updating the layer height command through in-machine probing between deposition layers can significantly improve process efficiency [15]. However, it should be noted that in-machine probing cannot provide real-time updates to the layer height command due to the need for material cooling before surface measurement can take place, thus, extending the overall manufacturing time. An alternative method of measuring part

Table 1 Review of approaches to predict DED bead height

Method	References
Empirically based coaxial monitoring system	[6,15,17]
Adaptive slicing	[18]
Lumped-parameter modeling	[19,20]
Finite element analysis	[21]
Analytically based coaxial triangulation monitoring and mass measurement system	[22]
Feedback-based coaxial monitoring system	[8,23–25]
Feedback-based coaxial and off-axial monitoring system	[10]
Feedback-based off-axial monitoring system	[26]
Feedback-based coaxial and triangulation monitoring system	[27]
In-machine probing	[15]
Structured laser light scanning	[16]
ML-based coaxial monitoring system	[14,28–31]
ML-based off-axial monitoring system	[12,32]
Multi-modal sensing	[33]
Destructive evaluation	[34,35]

geometry is structured 3D imaging [16], however, these methods are also not compatible with real-time control frameworks.

2.4 Review of Approaches to Predict Directed Energy Deposition Bead Height. Previously, there have been a wide variety of approaches to modeling and predicting bead height for DED using the different monitoring configurations discussed above. In this section, a brief overview of the strengths and weaknesses of the different approaches is presented and discussed. Table 1 outlines these approaches.

Approaches that seek to understand how process parameters change an outcome via experimentation are first discussed. For instance, Ocylok et al. used a coaxial camera to monitor the effect that varied process parameters has on melt pool geometry. Ocylock et al. found that laser power would be the best correcting variable for melt pool geometry control [36]. Moreover, Shim et al. used empirical methods to determine the layer height command [18] by creating an adaptive slicing strategy. This strategy was selected by a process diagram that displayed a single-layer height corresponding to the specific energy density of two combined parameters. Using this diagram, the part was then sliced based on the layer-specific depositing condition. A comparative analysis was conducted between this method, a closed-loop control method, and a conventional method (constant slicing thickness irrespective of process parameters). The comparative analysis was used to assess the performance of each method in terms of limiting over or under deposition during the build. Although closed-loop control was superior for geometric accuracy, the material properties were improved when using the adaptive slicing method. However, this method of open-loop control proposed by the adaptive slicing was only practical when the application was fixed and repeated over and over because identifying the right parameters required several combinations of experiments. Regrettably, empirical methods cannot be readily applied to different materials, part geometries, and machines without the need to repeat the experiments conducted to establish the original model. This process can consume significant resources and time.

Another set of approaches employed techniques that predict outcomes by utilizing equations that represent the underlying physics of the modeled situation. For example, finite element (FE) models are considered a physics-based model. However, FE models often use partial differential or difference equations, which due to their non-linear, time-dependent mathematical problem formulation often makes them challenging to implement for fine, real-time control. Utilizing physics-based lumped-parameter models and assumptions, on the other hand, are more control-friendly, but cannot predict part height as effectively [19,21]. At present, achieving accurate and rapid prediction of the entire AM process through physics-driven methods is not feasible.

Other studies created mathematical models that had a closed form solution. For instance, Donadello et al. created an analytical model to relate the powder catchment efficiency to the variation in process parameters as well as deposition height [22]. To evaluate the accuracy of the analytical model, a comprehensive experimental setup was necessary. The experimental setup consisted of a mass measurement system that monitored the quantity of powder deposited and the portion that was captured by the melt pool. Additionally, a coaxial optical triangulator was used to monitor layer height. The study showed that this model is feasible for an open-loop process optimization, due to its ability to accurately predict the deposition growth. Analytical models can demonstrate high effectiveness when applied to well-understood processes. However, they are not as effective as other methods in addressing process instability or irregular boundary conditions.

Among the various approaches, feedback-based methods were the most widely adopted for monitoring and control of the melt pool and layer height. The feedback-based approaches interpreted data from sensors and used statistically determined thresholds to determine how the machine should react. Feedback-based control is often categorized to be either fine or coarse. For instance, fine feedback control is typically used for real-time correction of process anomalies that can be measured in situ like melt pool temperature and geometry. Baraldo et al. demonstrated fine feedback control [8]. Baraldo et al. demonstrated how the image intensity from a thermal camera could be utilized to limit over-deposition on geometries, specifically, with small-angled corners. In contrast, coarse feedback is characterized by stopping the deposition and then correcting unfavorable process deviations in the next layer. In Garmendia et al. coarse feedback control was used to monitor build height between layers with a structured light 3D scanner. Based on the point cloud generated, the build path was corrected by either deleting or adding layers for improved control of final part geometry [16]. Another case of coarse feedback control utilized in-machine probing.

Lastly, ML-based approaches, also known as data-driven models, can be used to model and predict bead geometry. The significant advantage of this type of model lies in its ability to bypass the need for constructing an extensive list of physics-based equations. Instead, these models autonomously learn the correlation between input features and output targets through prior data. [35]. For example, ML models were used to detect geometric distortion using thermal history and provide feedback to rectify the issue in a computer aided design (CAD) model. Specifically for laser powder bed fusion, Francis et al. used a CNN to identify geometric distortion by analyzing thermal history and offer feedback to rectify the problem within a CAD model. Additionally, Zhang et al. utilized a CNN to monitor the melt pool, plume, and spatter [32]. Jamnikar et al. used multi-modal ML models, including a CNN-based model, that are trained on data collected from pyrometers, optical cameras, and acoustic sensors to predict bead geometry for a laser wire-feed DED system [14]. A few benefits of CNNs for process monitoring include: (1) high accuracy for quality identification, (2) no feature extraction step, and (3) great potential for real-time applications. Additionally, a benefit of using SVR is the model's quick training and inference time as well as strong ability to model non-linear relationships.

A shortcoming of both CNN and SVR models is the need for extensive amounts of data to train the model. In this regard, past work has not addressed the efficacy of edge compute compatible, lightweight models for inference of layer height in DED. In the present study, we are the first to have utilized melt pool data from a single, coaxial optical camera to train a CNN and SVR to predict DED bead height. Figure 1 displays the in situ coaxial monitoring that was used in this work. The impact of model size on classification performance was evaluated and implications for edge-based process control are discussed. Additionally, this paper provides novel insight and thorough exploration into the features that can be extracted from the image of the melt pool. This work is the first to explore using the reflection of the melt pool on the nozzle to indirectly infer layer height. Lastly, this paper also answers how those features can be used to improve model performance while minimizing model size and image processing time.

3 Methodology

In Sec. 3.1, the design of experiment is discussed. In Sec. 3.2, the methodology for data collection is outlined. Lastly, in Sec. 3.3, the model selection, architecture, and training are presented.

3.1 Design of Experiment. An Okuma MU-8000V LASER EX at Oak Ridge National Laboratory (ORNL) was the DED AM machine used to perform the experiments to collect training data for the ML algorithms. The MU-8000V LASER EX is hybrid manufacturing machine with an OSP-P300M controller. It has the capability of a computer numerical control (CNC) machine but it also has laser metal deposition abilities. This machine was equipped with a Kappa CF 8/5 MX monochrome camera with 12-bit digital signal processing and a MXC 200 controller. This camera had a frame rate of 30 fps and was mounted to the side of the deposition

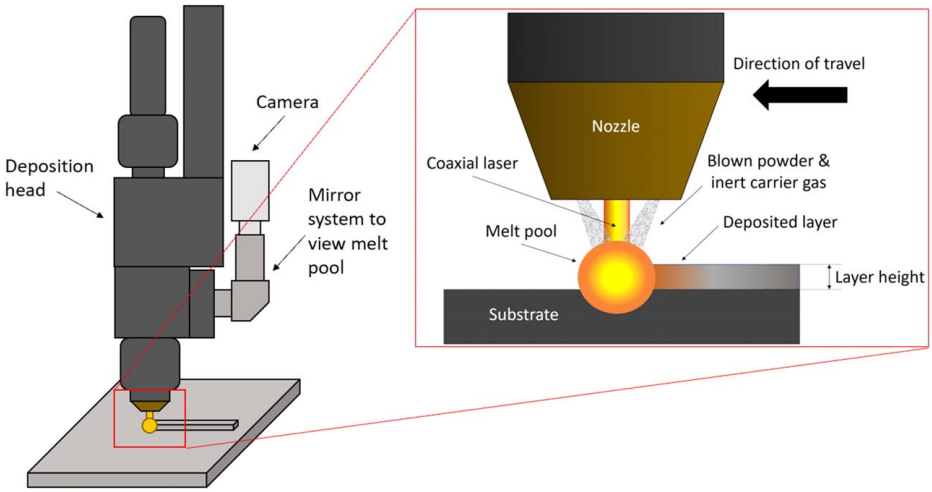

Fig. 1 Diagram of in situ coaxial monitoring of melt pool

head so that a set of mirrors could be used to view the melt pool in a coaxial manner. The camera was outfitted with a 1/2 in interline transfer charge-coupled device sensor with an area of 6.4 × 4.8 mm (752 × 582 pixels). To gather a training set for predicting layer height, a series of single-layer, single bead tracks were printed while varying the laser power. Laser power was selected as the independent variable for manipulation, as previous research has indicated that it exerts the most significant influence on layer height among all process parameters [36]. Throughout the experiments, all process parameters were maintained at a constant level while varying the laser power. Table 2 displays the process parameters used for the experiment. To capture potential deposition conditions, a large range of laser powers from 250 W up to 2500 W were tested. A hot-rolled steel plate 304.8 mm × 304.8 mm × 38.1 mm in size was used as the substrate for the deposition. The substrate print surface was machined flat before material deposition. Stainless steel (316L-D) powder from Oerlikon with a spheroidal morphology and nominal size range of $106 + / - 45$ μm was used. Custom G-code was created to increase or decrease laser power linearly with 23 mm between each programed laser power along a single-layer bead. Regions 7 mm long at the start and end of each track were not included in the analysis as these were found to exhibit clearly variable intensity and shape. A diagram of the process is shown in Fig. 2. The deposition began near the part origin in the lower left-hand corner of the plate as displayed in Fig. 2. As seen in Fig. 2, the laser power was increased from 250 to 2500 W. Once 2500 W was reached, it was decreased back to 250 W; this pattern was repeated over ten tracks. Researchers at ORNL conducted thorough material testing under various processing parameters and determined that a laser power of 2000 W was the recommended setting for this particular machine. Specifically, anything above 2000 W was found to result in cracking, whereas anything under 2000 W had porosity issues. To mitigate the influence of substrate temperature on bead geometry, the hot deposition head was temporarily relocated to a resting position away from the plate for approximately 3 min between each track. This allowed the plate to cool down during the time between depositions. Moreover, to minimize the effect of substrate temperature and location on bead geometry, the laser powers were repeated at different locations and in decreasing/increasing direction on the plate. A summary of the deposition path is outlined in Fig. 2 with a dashed line. Overall, the experiment was completed within 2 h. Delamination occurred at laser powers below 600 W because the laser did not have adequate power to create sufficient melt pool penetration into the substrate. To measure the geometry of the single-layer bead, a FARO Quantum Scan Arm with a certified resolution of 0.025 mm was employed at ORNL. The structured laser light scan of the plate conducted at ORNL was evaluated using GOM INSPECT, a software capable of assessing the dimensional accuracy of 3D-inspected parts. The mesh generated from the scan was compared to a CAD substrate that exhibited dimensional perfection. Figure 3 shows the geometric differences from the ideal, deposition-free substrate compared to the scanned mesh from the laser power experiment.

Table 2 Experimental process parameters

Process parameter	Value
Laser power	250–2500 W
Traverse speed	500 mm/min
Laser spot size	3.5 mm
Laser wavelength	1067 nm
Nozzle gas	15 L/min
Carrier gas	4 L/min
Powder mass flow	12 g/min
Standoff distance	12 mm
Run time	12 h

3.2 Data Collection and Processing. One significant limitation of supervised ML is the requirement for substantial amounts of labeled data. The process of labeling data can be costly and time-consuming. In response, a data pipeline was created for semi-automated data labeling. To label images based on layer height, it is essential to measure and record the layer height at various locations on the depositions in a manner that allows them to be linked to specific images of the melt pool. Performing this task manually would be time-consuming and could introduce significant human error depending on the chosen measurement technique. Thus, a software solution was developed to streamline the process. This software required only to input the .STL file from the structured laser light scanner and a .CSV file that contained the distance and number of plate cross sections to be analyzed. The computer program worked by slicing the experimental build with a distance between cross sections that corresponds to the rate at which the optical camera was able to capture a frame which was calculated to be 3.6 f/mm. Figure 4 shows an example of a slice corresponding to the cross section of a single bead. As can be seen in Fig. 2, 7 mm at the beginning and end of each bead was excluded from the dataset as the laser has not fully stabilized since being turned on/off. The height and width of each bead were found by fitting a second degree polynomial to the melt pool point cloud as can be seen in the example in Fig. 4. The width of each bead was found by finding the roots of where the average plate surface from a specific

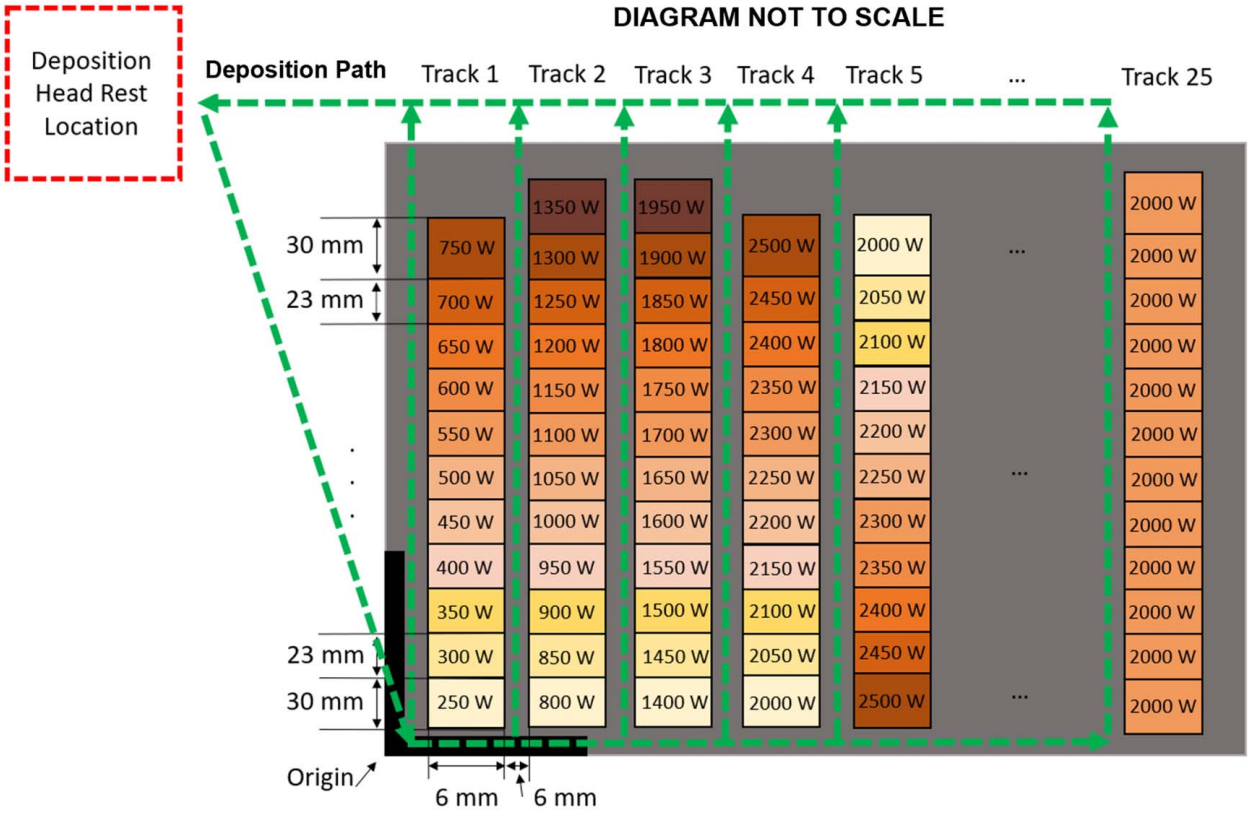

Fig. 2 Diagram of depositions from experiment

slice intersected with the second degree polynomial fit to the point cloud data that were determined to be in the melt pool. Overall, 7702 images were collected within tracks 1–10. Figure 5 displays a distribution of the height and width data collected. Additionally, the point cloud data from the experiment were also inspected using GOM INSPECT. The plate and the mesh generated from the scan were found to accurately represent the reality, as confirmed by a dial indicator.

In addition to the height and width data extracted from the point cloud, features extracted from each image were analyzed. Specifically, the melt pool and melt pool reflection of each image were analyzed to see if any extracted features correlated to final bead geometry. Table 3 displays the melt pool and melt pool reflection geometry extracted from each image for analysis. For the analysis displayed in Table 3, the melt pool was determined by binarizing the grayscale image with a threshold value of 180. An ellipse was then fit to the contour of the melt pool using a least-squares approach. An example of a fit ellipse with the first five features labeled is shown in Fig. 6(*a*). In addition, a rectangle was fit to the melt pool as can be seen in Fig. 6(*b*). For the melt pool reflection, two ellipses were fit as displayed in Fig. 6(*c*). One ellipse was fit to the inside, and another was fit to the outside. For each ellipse, the accuracy of the fit was included as a feature by calculating the root mean squared error between the fit ellipse and the melt pool contour. The error at each contour point was determined by drawing a line that passes through the ellipse center and the contour point. The error was the distance along that line between the ellipse and the contour.

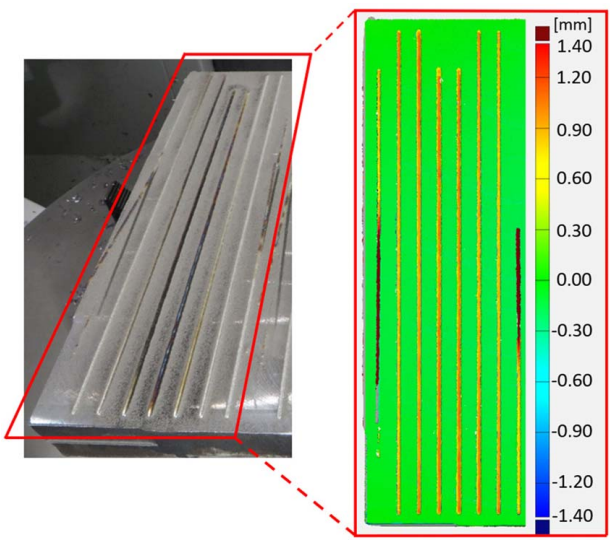

Fig. 3 Experiment after deposition and corresponding section of scanned geometry

In addition to analyzing the size and orientation of the melt pool and melt pool reflection, the texture of each image was analyzed in an attempt to capture information regarding the plume and spatter of the melt pool by calculating the statistical moments of the intensity histogram of each image. Specifically, the mean or average intensity (m), standard deviation or average contrast (σ), smoothness (R), third moment (μ_3), uniformity (U), and entropy (E) of each image were calculated. In order to calculate the statistical moments of the intensity histogram, let z be a random variable denoting intensity and let $p(z_i)$, $i = 0, 1, 2, \ldots, L-1$, be the corresponding normalized histogram components, where L is the number of distinct intensity levels. Equation (1) shows how to calculate the mean of an intensity histogram.

$$m = \sum_{i=0}^{L-1} z_i p(z_i) \tag{1}$$

Equation (2) displays how to calculate the standard deviation or average contrast of an intensity histogram where Eq. (3) shows

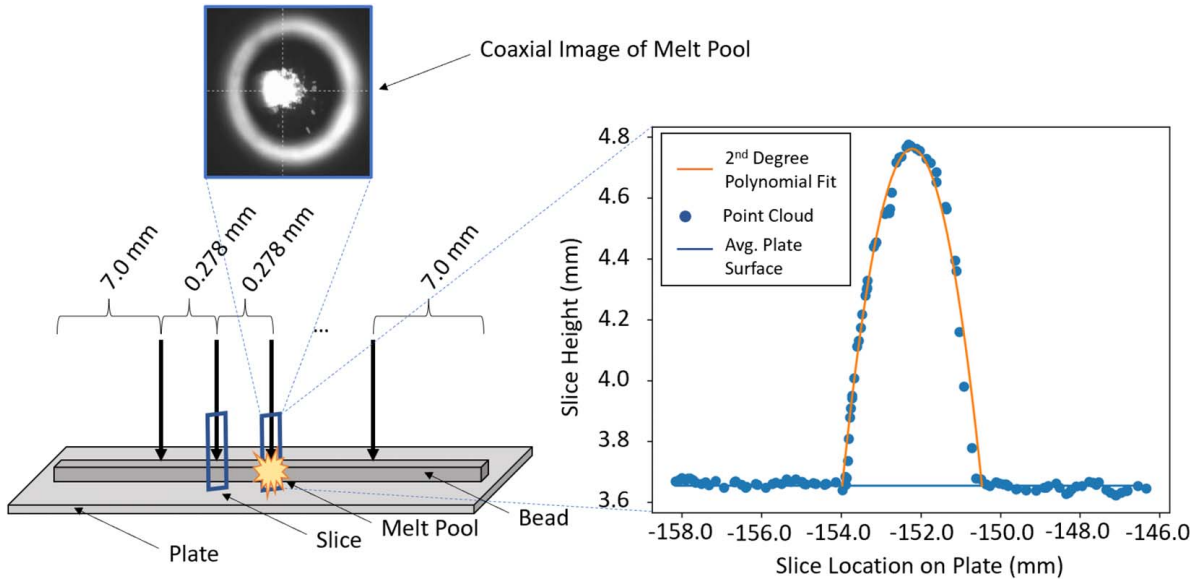

Fig. 4 Point cloud slicing methodology for data collection

how to calculate the nth moment of z about the mean.

$$\sigma = \sqrt{\mu_2} \tag{2}$$

The third moment quantifies the skewness of a histogram, indicating its asymmetry. A value of 0 for the third moment suggests a symmetric histogram, while positive values indicate a right-skewed histogram, and negative values indicate a left-skewed histogram.

$$\mu_n(z) = \sum_{i=0}^{L-1} (z_i - m)^n p(z_i) \tag{3}$$

Equation (4) was used to calculate the smoothness of an image. Smoothness is a measure of the relative smoothness of intensity within a region. A smoothness value of 0 indicates that the region of interest possesses a constant intensity. As the smoothness value (R) approaches 1, it indicates that the region of interest exhibits a wide range of intensity values with a chaotic distribution.

$$R = 1 - 1/(1 + \sigma^2) \tag{4}$$

Uniformity is expressed with Eq. (5). When all intensity values are the same, uniformity is maximum. Uniformity decreases from the maximum value as intensity values deviate from each other.

$$U = \sum_{i=0}^{L-1} p^2(z_i) \tag{5}$$

Lastly, Eq. (6) was used to calculate entropy. Entropy in an image is a measure of randomness.

$$E = -\sum_{i=0}^{L-1} p(z_i) \log_2 p(z_i) \tag{6}$$

In addition to the statistical moments of the intensity histogram, a measure called spatter (S) captures the pixels above a threshold of 180 outside of the melt pool and inside the reflection in an effort to capture the amount of spatter in an image.

3.3 Model Fitting, Evaluation, and Architecture. For modeling the final bead height, two models were explored. The first model explored was a CNN. A CNN was chosen due to its ability to model complex, non-linear data as well as its ability to perform automatic feature extraction via its convolution and pooling layers. A CNN consists of an input layer, a convolution layer, and pooling layer, and towards the end of a CNN is a fully connected layer [37]. The input layer represents the input image into the CNN. The input images were normalized and rescaled from 0–255 to 0–1. After the input layer, a convolution layer in the CNN model was used to extract features from an input image. An activation function was applied to the convolutional layer. Without an activation function, the CNN would not perform well in a non-linear environment. A ReLU activation function was used in this model and represented in Eq. (7).

$$\mathrm{ReLU}(x) = \max(0, x) \tag{7}$$

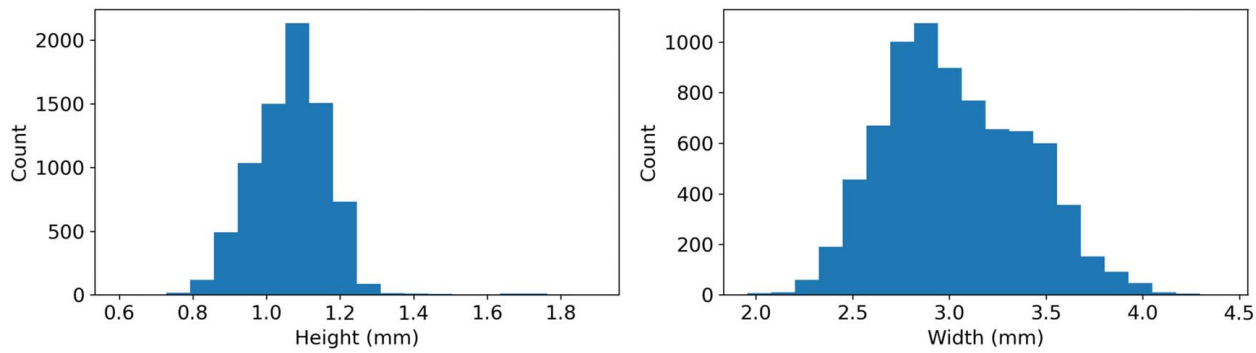

Fig. 5 Histogram of collected height and width data

Table 3 Description of extracted melt pool and melt pool reflection features

Symbols	Description
x_{mp}, x_{ir}, x_{or}	X-coordinate of center of fit ellipse on melt pool, inner reflection, and outer reflection
y_{mp}, y_{ir}, y_{or}	Y-coordinate of center of fit ellipse on melt pool, inner reflection, and outer reflection
a_{mp}, a_{ir}, a_{or}	Major axis (half-length) of fit ellipse on melt pool, inner reflection, and outer reflection
b_{mp}, b_{ir}, b_{or}	Minor axis (half-length) of fit ellipse on melt pool, inner reflection, and outer reflection
θ_{mp}, θ_{ir}, θ_{or}	Rotation angle of fit ellipse on melt pool, inner reflection, and outer reflection
e_{mp}, e_{ir}, e_{or}	Error in the fit ellipse on melt pool, inner reflection, and outer reflection
NOP_{mp}, NOP_r	Number of pixels in melt pool and melt pool reflection
$NOP_{>th}$	Number of pixels inside reflection above a threshold of 180
h_{rec}, w_{rec}	Height and width of rectangle fit to melt pool
x_{rec}, y_{rec}	X and Y coordinates of rectangle fit to melt pool (located at the bottom-right of fit rectangle)

ReLU stands for a rectified linear unit and it is a popular activation function due to its ability to converge quickly and prevent the vanishing gradient problem. Following the convolution step, a pooling layer was utilized to reduce the spatial dimension of the network. This pooling layer decreased the number of parameters and overall computational complexity of the network. Specifically, a max pooling layer was chosen for the CNN architecture. While designing the CNN's architecture, one must select the kernel size and stride length for the max pooling operation. The max pooling operation involves sliding the designated kernel with the specified stride over the input, while choosing the maximum value within the kernel. This process results in an output with a smaller size compared to the input. Lastly, the fully connected layer receives an input volume that is equal to the proceeding output of the convolution, activation function, or pooling layer. It generates an N-dimensional vector where N is equal to the number of values being predicted. The output is obtained by subjecting the inputs to a linear activation function. This algorithm was used to calculate a final bead height value and allows one to use a CNN for regression. The loss function that is minimized in this model for regression is the mean squared error (MSE). The architecture of the CNN model used for modeling bead height is pictured in Fig. 7. CNNs come in many different architectures to suit different needs. Due to the need for real-time bead height prediction on an edge device, a CNN with a relatively small number of model parameters was chosen. The CNN model trained used a Glorot uniform initalizer, Adam optimization, and early stopping to prevent overfitting. The second model chosen to model final bead geometry was a ϵ-SVR model [38]. The SVR model was created by Vapnik in 1995 and creates a model by fitting a hyperplane to the data so that the maximum number of training observations are within the margin and observations outside of the margin (slack variables) are penalized [39]. The validity of each model was tested using k-fold ($k = 5$) cross validation which is a popular method for the evaluation of model performance [40]. Before model training, 10% of the data was randomly withheld for final testing. The remaining data were randomly divided into five folds so that 18% of the data was included in each fold. Additionally, the hyperparameters used in each model were tuned using a grid search. For a CNN, the hyperparameters that were tuned refer to batch size and learning rate. For SVR, the hyperparameters that were tuned refer to the kernel coefficient for the radial basis function (gamma) and regularization (C). All models were trained and evaluated on a computer with a NVIDIA Tesla P40 graphics processing unit and an Intel Xeon Gold 6140 processor.

In the next section, each extracted feature was analyzed to better understand its relationship, if any, to final bead height and width. This process was used to guide feature selection for the models created to predict final bead geometry.

4 Results and Discussion

4.1 Image Processing Results. The features extracted from the image were done so in an attempt to better understand the relationship between the images and final bead height. Overall, almost all of the extracted features from the melt pool images when compared to bead height were non-linear. Figure 8 displays the connection between laser power and height. From this figure, one can see that height increases linearly with laser power up until 2150 W and then height starts to decrease because the higher laser power increases the bead dilution and depth on penetration into the build plate. As a result, the width of the bead increases and the height of the bead decreases. This trend was also observed in the work completed by Shim et al. [18]. Figure 9 displays the features extracted from the melt pool. The features from the fit ellipse and rectangle follow the same trend of slowly increasing after a height value of 1.07 mm. This height value corresponds to a laser power greater than 1200 W. The height of the bead and the size

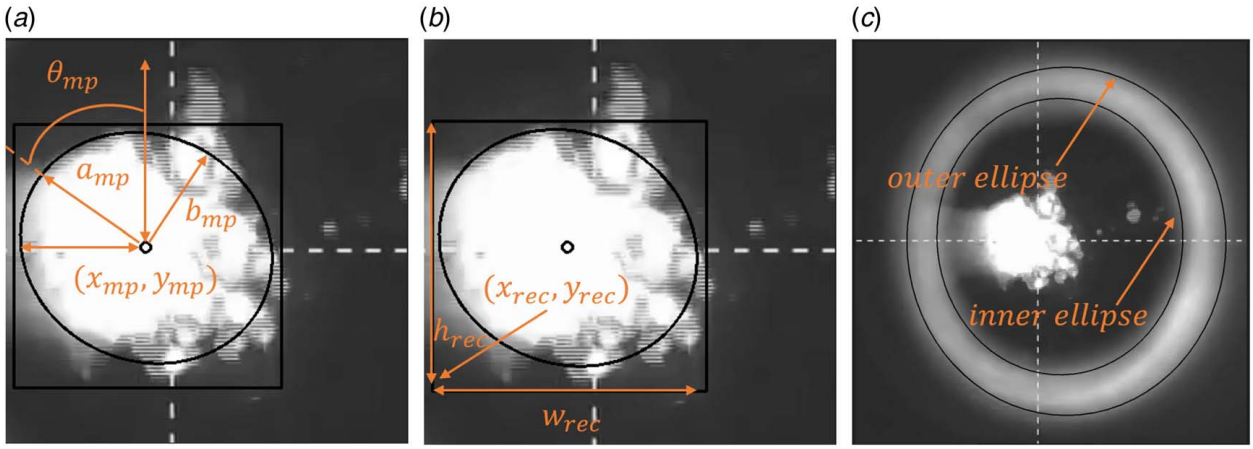

Fig. 6 Extracted melt pool and melt pool reflection geometry

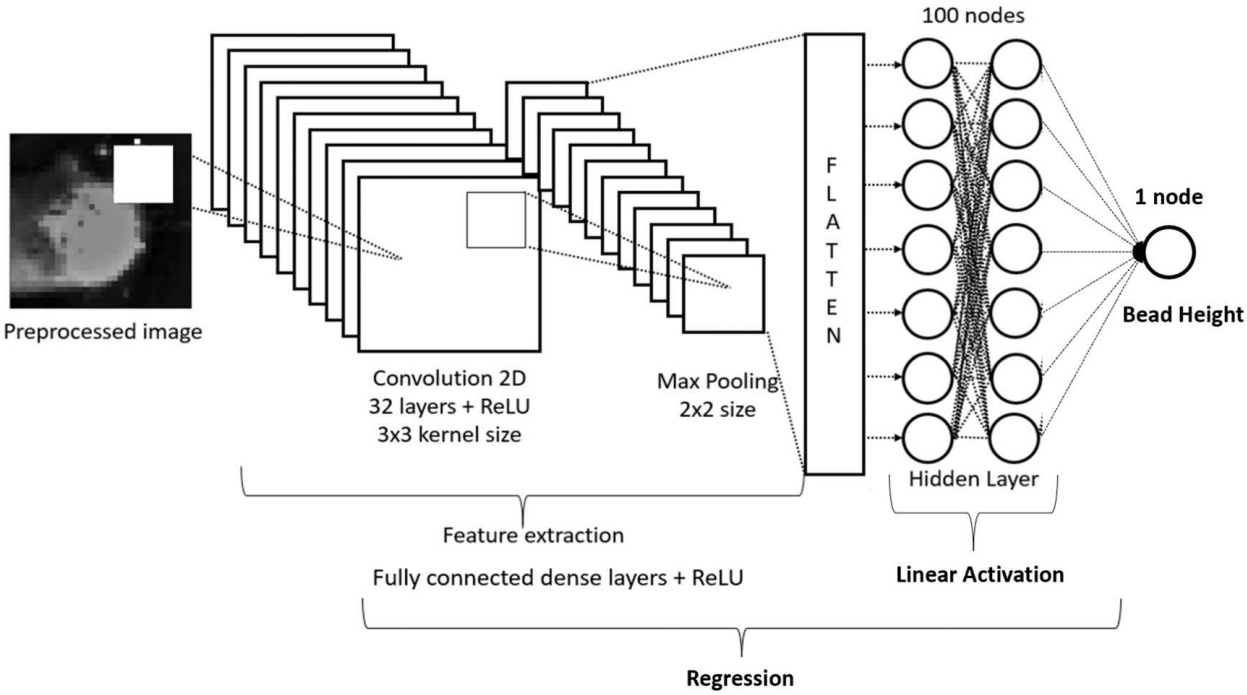

Fig. 7 CNN architecture

of the melt pool increasing after this laser power make sense as it is getting closer to the ideal laser power of 2000 W for optimal powder capture efficiency and thus a taller bead. Figure 10 displays the features extracted from the inner and outer ellipse of the melt pool reflection. Interestingly, a similar pattern of a quicker increase around a height of 1.07 mm followed by a slower increase can be seen for the major and minor axes of the ellipse fitted to the outer reflection. Interestingly, around the same height value, there was a decrease in the major and minor axes of the inner reflection. In addition, Fig. 10 shows that the inner reflection ellipse-fit error started to increase after a height of 1.07 mm, thus capturing the change in melt pool reflection at this point. There was little change in the values of the center of both the inner and outer reflection as well as ellipse orientation. Figure 11 displays the graphs for spatter, number of pixels above a threshold of 180, number of pixels in the melt pool, number of pixels in the reflection, the ellipse-fit error for the melt pool, and the rotation of the ellipse fit to the melt pool, respectively. As expected, the features that measure the size of the melt pool and melt pool reflection increased after a height of 1.07 mm. Interestingly, at this point, the error of the ellipse fit of the melt pool was at a minimum at 1.07 mm. This momentary decrease in eccentricity could have been a result of the laser operating in the recommended deposition range, thus, resulting in more circular melt pools due to optimal laser and process parameters. At around heights similar to those created at 2300 W, the eccentricity increased, as the laser power exceeded the optimal deposition range.Figure 12 displays the features extracted from the image for texture analysis. The average intensity (m), uniformity (U), entropy (E), and the third moment (μ_3) all display a similar pattern to what is seen when analyzing the features extracted from the melt pool. Additionally, entropy was collected as a measure of randomness in an image. Before these experiments, it was thought that entropy may detect spatter resulting from inadequate powder capture due to insufficient laser powder. As seen in Fig. 12, entropy was stable, and then it decreased linearly until it appeared to stabilize around the tallest bead heights. This could have been due to better powder capture and less spatter. It could also have been a result of the increasing size of the melt pool and nozzle reflection, which both would have increased entropy since these features have constant intensity values. Additionally, the image data captured from the laser power study can aid one in understanding the general trends and characteristics of the data used to train a model. Due to the overall non-linear nature of the image data, a CNN and SVR were chosen as the models for comparison. A CNN was chosen due to its ability to perform well when modeling complex, non-linear data. It was also chosen because a CNN is able to automatically learn the most important features in an image and does not require feature extraction and certain image or melt pool proprieties. Additionally, an SVR was

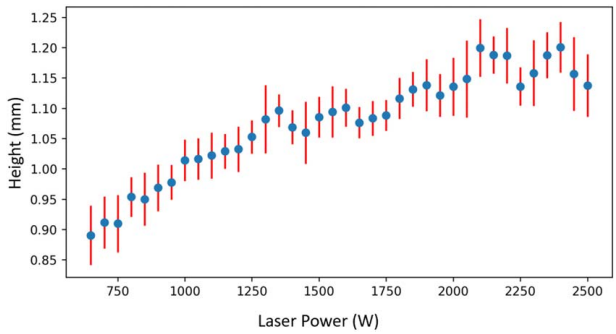

Fig. 8 Height (mm) versus laser power (W). The error bars in the figure represent one standard deviation.

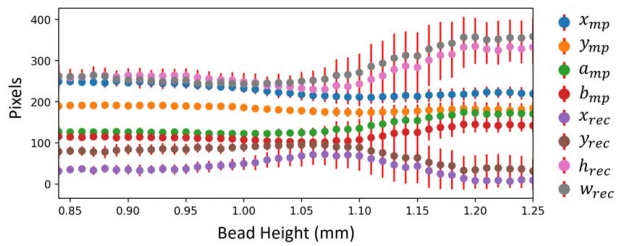

Fig. 9 Features extracted from melt pool geometry (pixels) versus bead height (mm). The error bars in the figure represent one standard deviation.

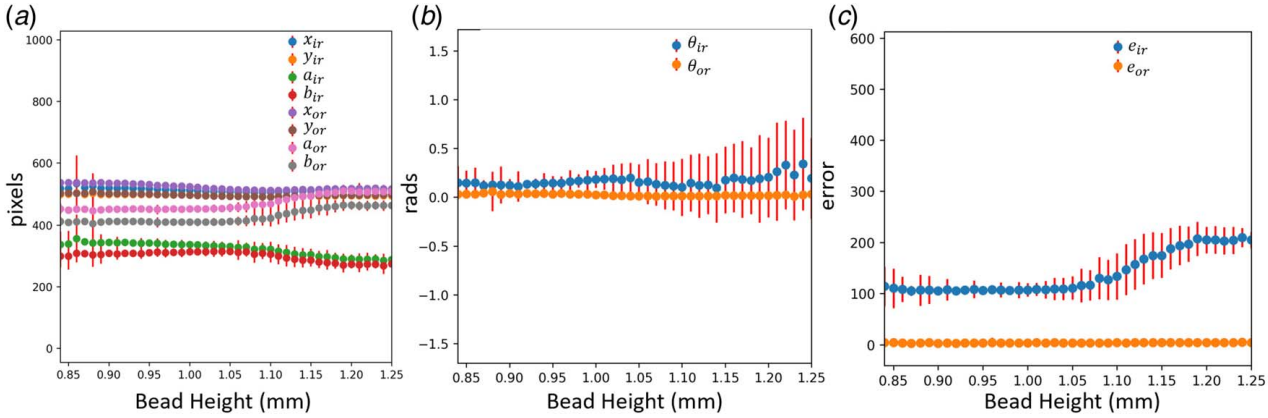

Fig. 10 (*a*) Features extracted from melt pool reflection geometry (pixels) versus bead height (mm). (*b*) Rotation angle of fit ellipse on melt pool reflection (rad) versus bead height (mm). (c) Error in the fit ellipse on melt pool reflection (pixels) versus bead height (mm). The error bars in the figure represent one standard deviation.

chosen for its ability to work well on non-linear problems and its ability to be non-biased by outliers.

4.2 Feature Selection Using Gini Importance. After all features were extracted, they were standardized so that they had zero mean and unit standard deviation. To determine the most important features, the 32 features were run through a random forest (RF) regressor. RF regressors can be used to determine feature importance by measuring the impurity reduction of splits, also known as calculating the Gini importance [41]. The most important features were selected, which will be discussed later in the paper, and fed into a SVR model to predict the final bead geometry. By using a RF regressor to calculate feature importance and a SVR for inference, one can achieve some explainability without sacrificing model performance [42]. Figure 13 displays the Gini feature importance calculated for predicting the bead height. The inner reflection ellipse-fit error (e_{ir}) had the highest Gini feature importance thus suggesting that this feature contributed significantly to predicting bead height. This could be a result of the fact that e_{ir} began to increase and then level off after a height value of 1.05 mm. This trend can be seen in other extracted features from the images, however, e_{ir} had the tightest error bounds, which could be why this particular feature contributed significantly to the bead height prediction.

4.3 Support Vector Regression Results. Unlike a CNN, a SVR model requires features to be extracted from the image before training. In order to find the optimal number of features to have the most accurate prediction for the least number of features, SVR models were trained with an increasing number of features added each time in the order of feature importance. The results of this training can be seen in Fig. 14. Figure 14 shows the number of features added in the order of decreasing feature importance. For example, the SVR with only one

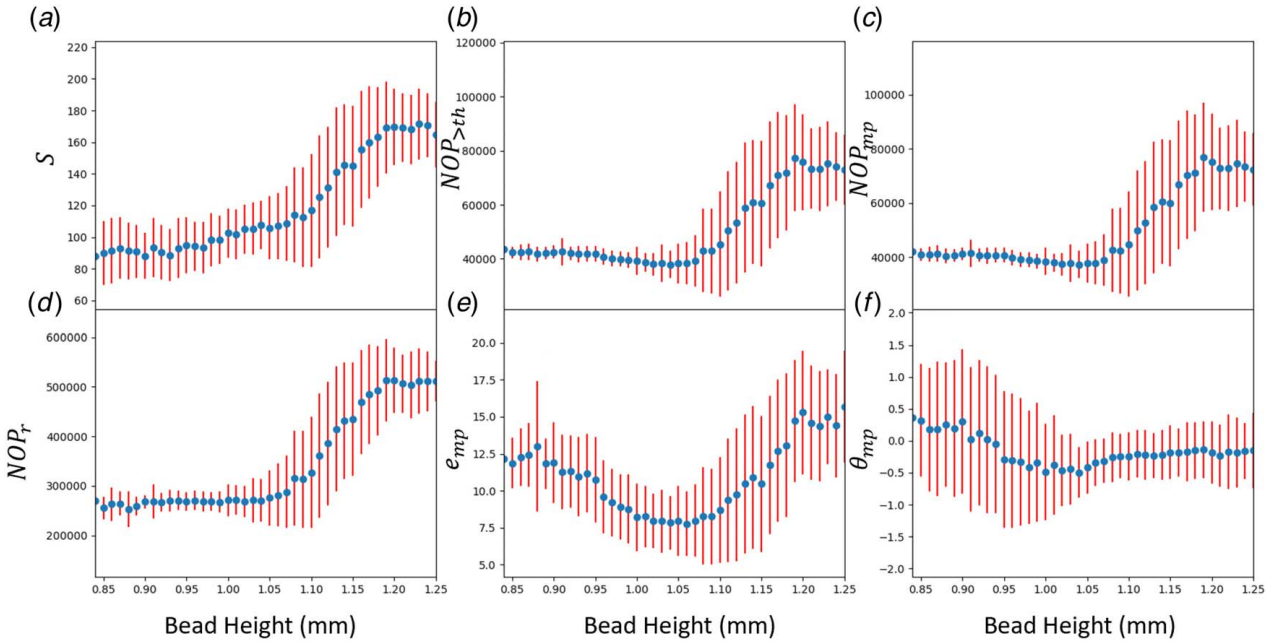

Fig. 11 (*a*) Spatter versus bead height (mm). (*b*) Number of pixels inside reflection above a threshold of 180 versus bead height (mm). (c) Number of pixels in melt pool versus bead height (mm). (*d*) Number of pixels in melt pool reflection versus bead height (mm). (*e*) Error in the fit ellipse on melt pool versus bead height (mm). (*f*) Rotation angle of ellipse fit on melt pool (rad) versus bead height (mm). The error bars in the figure represent one standard deviation.

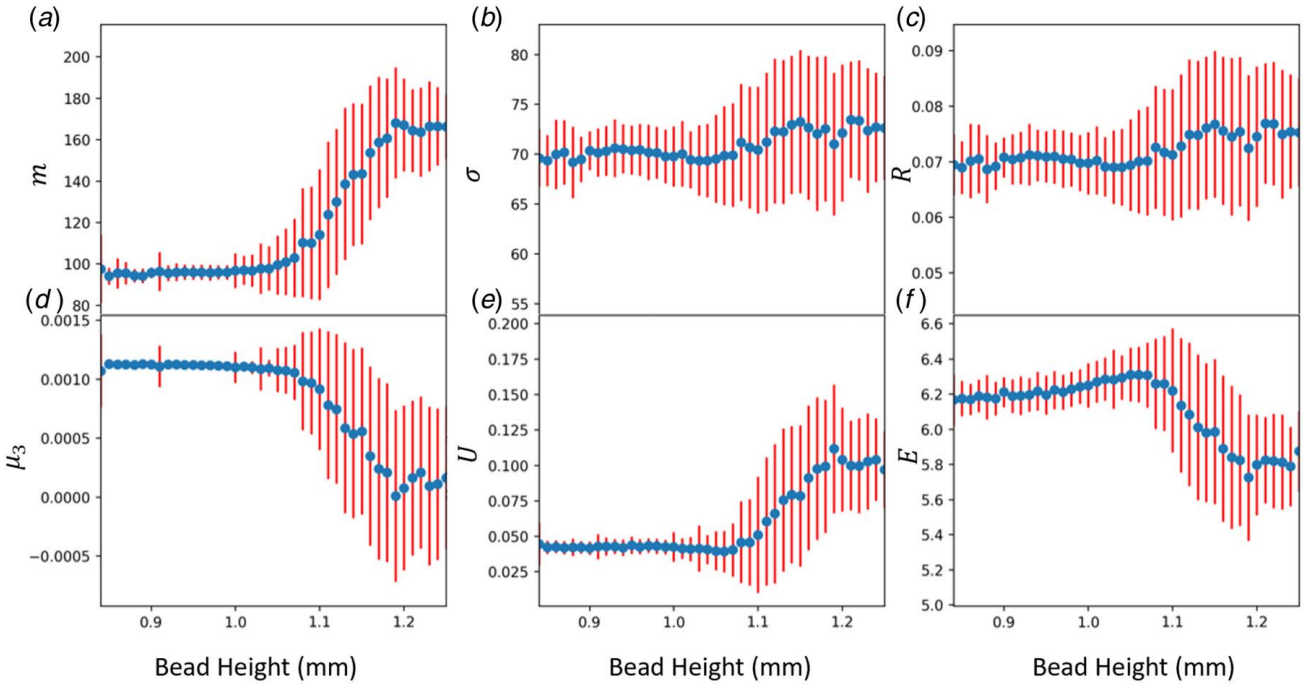

Fig. 12 (*a*) Mean of intensity histogram versus bead height (mm). (*b*) Standard deviation of intensity histogram versus bead height (mm). (c) Smoothness versus bead height (mm). (*d*) Third moment of intensity histogram versus bead height (mm). (e) Uniformity versus bead height (mm). (*f*) Entropy versus bead height (mm). The error bars in the figure represent one standard deviation.

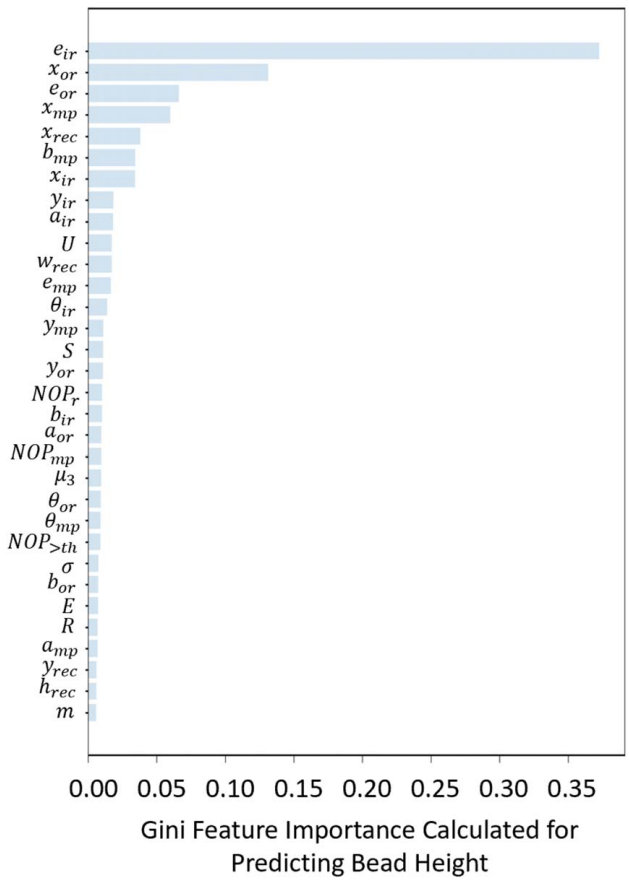

Fig. 13 Gini feature importance for features extracted from image used to predict bead height

feature used e_{ir} only. With only one feature, the SVR was still able to achieve good validation results of a MAPE of 5.87%. With all 32 features, the SVR was able to achieve a validation score of 3.93%. Table 4 displays the grid search used for tuning C and gamma hyperparameters. The regularization parameter determined the amount of acceptable error; this parameter controlled the trade-off between the maximization of the margin around the decision boundary (lower C) and the correct classification of training data points (higher C) [41]. Gamma determined the influence of an individual training data point (low values mean that the radius of influence associated with the data point is large). All combinations of gamma and C values of interest were tested, and the mean accuracy across five folds was evaluated. A radial basis function (RBF) kernel was used for all models due to the complexity of the image data. After performing the grid search, it was found that a value of $C = 1$ and gamma $= 0.01$ resulted in the lowest average MAPE over five folds.

In Fig. 14, one can see that a SVR trained on all features performed better than an SVR trained on one or two features. However, this performance improvement comes with a cost. Extracting more features from the melt pool image increased the

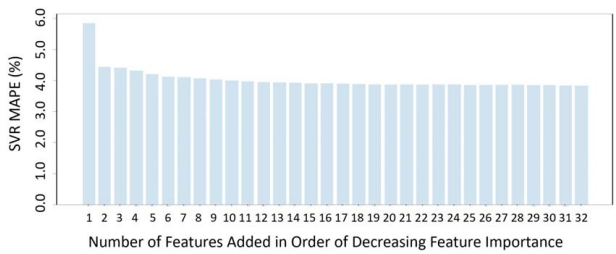

Fig. 14 SVR MAPE (%) versus number of features added in order of decrease feature importance

Table 4 SVR (all features) hyperparameter tuning

Gamma	C	Avg. MAPE (%)	Std. dev.
0.01	100	4.22	0.07
0.01	10	4.06	0.18
0.01	1	3.98	0.18
0.1	100	4.13	0.30
0.1	10	4.18	0.29
0.1	1	4.16	0.27
1	100	4.32	0.47
1	10	4.44	0.54
1	1	4.53	0.58

Table 5 Experiment process parameters

Features	Average feature extraction time per image (s)
x_{mp}, y_{mp}, a_{mp}, b_{mp}, θ_{mp}, x_{rec}, y_{rec}, h_{rec}, w_{rec}	0.0337
e_{mp}	0.0339
m, σ, μ_3, R, U, E	0.0010
S	0.0502
$NOP_{>th}$	0.0003
NOP_{mp}	0.0329
NOP_r	0.0055
x_{ir}, y_{ir}, a_{ir}, b_{ir}, θ_{ir}	0.0385
e_{ir}	0.0351
x_{or}, y_{or}, a_{or}, b_{or}, θ_{or}	0.0384
e_{or}	0.0352

feature extraction time, which increased the inference time for real-time prediction and control of bead height. To quantify this tradeoff, the average feature extraction time per image for each feature was measured and is shown in Table 5. In Table 5, features are grouped together if the main calculation was done once for all of them. The most time-consuming feature to calculate was spatter. From Fig. 13, one can see that spatter did not contribute significantly to the feature importance and in Fig. 14 one can see that it does not notably decrease MAPE. Thus, knowing this information is important and can be used to create smaller, faster models for real-time bead height monitoring and control. Since the decrease in MAPE after training an SVM with the top six features was not significant, the overall feature extraction time for the SVR model was significantly reduced from 0.307 s to 0.1344 s. In the next section, the results from training a CNN are discussed.

Table 6 CNN hyperparameter tuning for uncropped image

Batch size	Learning rate	Average MAPE (%)	Std. dev.
32	0.0001	3.69	0.350
32	0.001	5.29	1.90
32	0.01	9.47	4.93
64	0.0001	3.89	0.475
64	0.001	6.85	1.53
64	0.01	5.66	1.20
128	0.0001	3.71	0.223
128	0.001	6.80	1.68
128	0.01	7.54	0.112
256	0.0001	3.60	0.158
256	0.001	6.93	1.44
256	0.01	7.64	0.192

Table 7 CNN hyperparameter tuning cropped image

Batch size	Learning rate	Average MAPE (%)	Std. dev.
32	0.0001	4.27	0.313
32	0.001	6.99	1.25
32	0.01	7.64	0.189
64	0.0001	4.15	0.260
64	0.001	7.64	0.159
64	0.01	7.63	0.269
128	0.0001	4.23	0.180
128	0.001	7.64	0.135
128	0.01	7.63	0.204
256	0.0001	4.03	0.308
256	0.001	7.64	0.0845
256	0.01	7.64	0.0700

4.4 Convolutional Neural Network for Regression Results. To tune the models, five-fold cross validation was used with a grid search to optimize the selection of the learning rate and batch size hyperparameters for a $64 \times 64 -$ pixel input image. A $64 \times 64 -$ *pixel image* was selected for training since it was the smallest sized image that did not significantly loose information when viewed by a human. As the CNN model could potentially be deployed on edge devices to predict layer height for feedback-based machine control, it was essential to have a smaller model size suitable for such devices. The size of the input image significantly impacts the number of parameters in the model, which in turn affects the required random-access memory (RAM) and graphics processing unit (GPU) power necessary to run the model for inference.

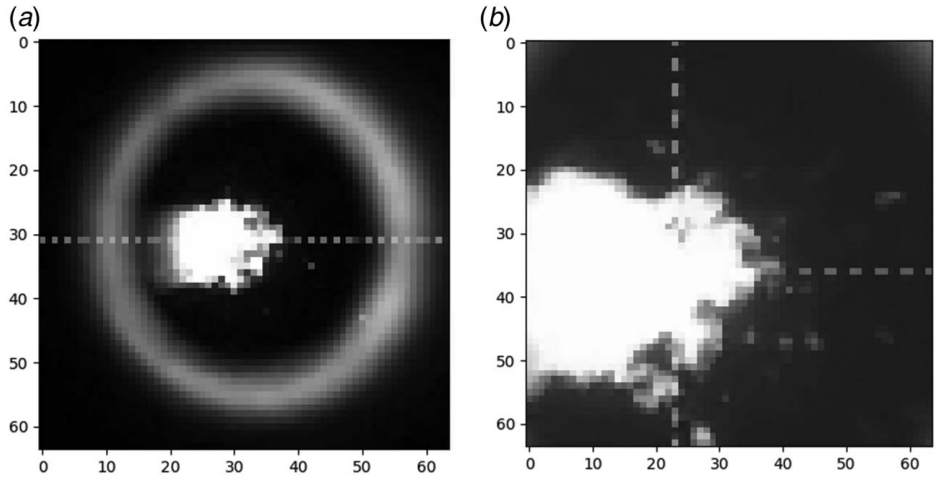

Fig. 15 64 × 64 pixel uncropped (*a*) and cropped (*b*) images of melt pool

Table 8 Model memory and computational time comparison

Model	Features	Model size	Preprocessing time per image (s)	Inference time per image	Total time per image (s)	Test MAPE (%)
CNN	Cropped 64 × 64 × 1 image	35.3 MB	0.000225	0.0019	0.00213	4.21
CNN	Uncropped 64 × 64 × 1 image	35.3 MB	0.000174	0.0019	0.00207	3.69
SVR	All	65 KB	0.3074	0.00	0.307	3.67
SVR	Top 6	20 KB	0.1344	0.00	0.134	3.86

Additionally, two CNN models were trained. One was trained with uncropped images of the melt pool as can be seen in Fig. 15 and the other was trained with cropped images of the melt pool. This was done to see if the reflection contributed valuable information that would help more accurately predict bead height. Little is known in the literature regarding how the melt pool reflection is related to final part geometry. The values chosen for each of the hyperparameters in the grid search were chosen based on past experience. Based on the results in Table 6, one can see that the lowest MAPE across five folds was achieved with a learning rate of 0.0001 and a batch size of 256. The learning rate hyperparameter controlled the rate or speed at which the model learned. Additionally, batch size refers to the number of training examples utilized in a single iteration of training prior to updating the model. Table 7 displays the batch sizes and learning rates used for tuning the model trained on the cropped images of the melt pool. The best MAPE score achieved during hyperparameter tuning over five folds was 4.03 with a batch size of 256 and a learning rate of 0.001. The grid search showed that the same batch size and learning rate performed best for both the uncropped and cropped image models. This makes sense because the dimensionality of the data and the model architecture remained the same between both models. However, the validation MAPE resulting from hyperparameter tuning was lower for the model trained on uncropped images, thus suggesting that the reflection of the melt pool did provide valuable information for accurately predicting bead height. After hyperparameter tuning, the models were tested on the data in the test set to understand how the models performed on unseen data. In the next section, the performance of the SVR and CNN models are compared.

4.5 Model Performance Comparison. For a model to be feasible for real-time bead height monitoring and control in a production environment, it must be able to perform inference quickly and be small enough to be executed on an edge device. For example, a DED machine moving at a traverse speed of 500 mm/min with a laser power of 2000 W would need an inference time of less than 0.34 s to be able to control the bead height within the average width of a single bead which was measured to be 2.8 mm. Thus, the ideal model is small and fast. For metal AM, a reasonable tolerance is plus or minus 0.1 mm. Thus, any MAPE under 10% will allow the machine to successfully control bead height. Based on this requirement, one can see in Table 8 that all four models met the requirements for inference speed and a MAPE of under 10% on a test dataset. Additionally, all models were sufficiently small and could easily fit on an edge device. The SVR trained on only six features was found to be the smallest model, however, the test MAPE was not as low as the SVR trained on all features, which has the lowest test MAPE and thus the best performance across all models. However, the SVR trained on all features has the highest preprocessing time per image, thus resulting in the highest inference time. The 0.307 s processing time still allows for inference within a single melt pool, however, it is close to the limit of a 0.34 s inference speed for real-time prediction and control. When considering the overall performance, the best two models were the CNN trained on the uncropped images and the SVR trained on all of the features. If smallest inference time is considered most important, then the CNN trained on uncropped images performed best. If an accurate prediction of bead height is considered more important than inference speed, then the SVR trained on all images was found to be the best model. Additionally, all models performed better than the 8.04% error reported from the CNN-based sensing-geometry model trained to predict wire-fed DED layer height by Jamnikar et al. [14].

5 Conclusion

In conclusion, this work presented a novel way to indirectly measure bead height from a coaxial image of the melt pool using a CNN and SVR with a MAPE of 3.68% and 3.67%, respectively. This experiment proves that both SVR and CNN models can model bead height based on only information from an overhead image of the melt pool. A SVR allows for a smaller model but larger image preprossessing time per image. This time is greatly reduced using feature importance to reduce the number of features trained in the SVR thus reducing the inference time by more than half with a small increase in MAPE. Moreover, this research shows that bead height can be identified from melt pool imaging within a range less than the tolerance of most metal AM machines (+/ − 0.1 mm). Furthermore, this study presents a data collection pipeline that facilitates rapid gathering of training data for models. This pipeline not only enables non-contact, real-time measurement of bead height but also offers seamless and cost-effective integration with the machine using a coaxial camera. Unlike comparable solutions, this setup eliminates the need for filters, calibration, or waiting for the part to cool before measurements can be obtained. Moreover, this investigation demonstrated that the proposed model can be executed on an edge device to facilitate closed-loop or feedforward control. This is possible thanks to its compact model size, rapid inference speed, and capacity to yield satisfactory outcomes with small input images. The model was developed using TensorFlow, making it compatible with contemporary edge devices such as NVIDIA's Jetson TX2. Therefore, the ability to detect bead height in real-time will result in improved overall part dimensional accuracy. Future work will focus on addressing situations not considered here, including expanding the model to address transient regions at the start and end of a bead as well as in multi-bead depositions.

Acknowledgment

This work was supported by the U.S. Department of Energy, Office of Science, Office of Advanced Materials and Manufacturing Technologies under contract number DEAC05-00OR22725, the Department of Energy through award DEEE0008303, and by a National Science Foundation Graduate Research Fellowship to ZA. The authors would also like to thank the Okuma America Corporation for their support of this project.

Conflict of Interest

There are no conflicts of interest.

Data Availability Statement

The datasets generated and supporting the findings of this article are obtainable from the corresponding author upon reasonable request.

References

[1] Frazier, W. E., 2014, "Metal Additive Manufacturing: A Review," J. Mater. Eng. Perform., **23**(6), pp. 1917–1928.

[2] Schmidt, M., Merklein, M., Bourell, D., Dimitrov, D., Hausotte, T., Wegener, K., Overmeyer, L., Vollertsen, F., and Levy, G. N., 2017, "Laser Based Additive Manufacturing in Industry and Academia," CIRP Ann., **66**(2), pp. 561–583.

[3] Kaierle, S., Overmeyer, L., Alfred, I., Rottwinkel, B., Hermsdorf, J., Wesling, V., and Weidlich, N., 2017, "Single-Crystal Turbine Blade Tip Repair by Laser Cladding and Remelting," CIRP J. Manuf. Sci. Technol., **19**, pp. 196–199.

[4] Bikas, H., Stavropoulos, P., and Chryssolouris, G., 2016, "Additive Manufacturing Methods and Modelling Approaches: A Critical Review," Int. J. Adv. Manuf. Technol., **83**(1–4), pp. 389–405.

[5] Bourell, D., Kruth, J. P., Leu, M., Levy, G., Rosen, D., Beese, A. M., and Clare, A., 2017, "Materials for Additive Manufacturing," CIRP Ann., **66**(2), pp. 659–681.

[6] Vandone, A., Baraldo, S., Valente, A., and Mazzucato, F., 2019, "Vision-Based Melt Pool Monitoring System Setup for Additive Manufacturing," Procedia CIRP, **81**, pp. 747–752.

[7] Boddu, M., Landers, R., and Liou, F., 2001, "Control of Laser Cladding for Rapid Prototyping—A Review," In Proceedings of the 12th Annual Solid Freeform Fabrication Symposium, Austin, TX, Aug. 6–8, pp. 460–467.

[8] Baraldo, S., Vandone, A., Valente, A., and Carpanzano, E., 2020, "Closed-Loop Control by Laser Power Modulation in Direct Energy Deposition Additive Manufacturing," Proceedings of 5th International Conference on the Industry 4.0 Model for Advanced Manufacturing, Belgrade, Serbia, June 1–4, L. Wang, V. D. Majstorovic, D. Mourtzis, E. Carpanzano, G. Moroni, and L. M. Galantucci, eds., Springer International Publishing, Cham, pp. 129–143.

[9] Song, L., and Mazumder, J., 2011, "Feedback Control of Melt Pool Temperature During Laser Cladding Process," IEEE Trans. Control Syst. Technol., **19**(6), pp. 1349–1356.

[10] Sun, Z., Guo, W., and Li, L., 2020, "In-Process Measurement of Melt Pool Cross-Sectional Geometry and Grain Orientation in a Laser Directed Energy Deposition Additive Manufacturing Process," Opt. Laser Technol., **129**, p. 106280.

[11] Herman, I. P., 1996, *Optical Diagnostics for Thin Film Processing*, Academic Press, San Diego, CA.

[12] Jiao, W., Wang, Q., Cheng, Y., and Zhang, Y., 2021, "End-to-End Prediction of Weld Penetration: A Deep Learning and Transfer Learning Based Method," J. Manuf. Process., **63**, pp. 191–197.

[13] Donadello, S., Motta, M., Demir, A. G., and Previtali, B., 2018, "Coaxial Laser Triangulation for Height Monitoring in Laser Metal Deposition," Procedia CIRP, **74**, pp. 144–148.

[14] Jamnikar, N. D., Liu, S., Brice, C., and Zhang, X., 2022, "In-Process Comprehensive Prediction of Bead Geometry for Laser Wire-Feed DED System Using Molten Pool Sensing Data and Multi-modality CNN," Int. J. Adv. Manuf. Technol., **121**(1–2), pp. 903–917.

[15] Kono, D., Yamaguchi, H., Oda, Y., and Sakai, T., 2020, "Stabilization of Standoff Distance by Efficient and Adaptive Updating of Layer Height Command in Directed Energy Deposition," CIRP J. Manuf. Sci. Technol., **31**, pp. 244–250.

[16] Garmendia, I., Leunda, J., Pujana, J., and Lamikiz, A., 2018, "In-Process Height Control During Laser Metal Deposition Based on Structured Light 3D Scanning," Procedia CIRP, **68**, pp. 375–380.

[17] Kledwig, C., Perfahl, H., Reisacher, M., Brückner, F., Bliedtner, J., and Leyens, C., 2019, "Analysis of Melt Pool Characteristics and Process Parameters Using a Coaxial Monitoring System During Directed Energy Deposition in Additive Manufacturing," Materials, **12**(2), p. 308.

[18] Shim, D.-S., Baek, G.-Y., Seo, J.-S., Shin, G.-Y., Kim, K.-P., and Lee, K.-Y., 2016, "Effect of Layer Thickness Setting on Deposition Characteristics in Direct Energy Deposition (DED) Process," Opt. Laser Technol., **86**, pp. 69–78.

[19] Li, J., Wang, Q., Michaleris, P. P., Reutzel, E. W., and Nassar, A. R., 2017, "An Extended Lumped-Parameter Model of Melt–Pool Geometry to Predict Part Height for Directed Energy Deposition," ASME J. Manuf. Sci. Eng., **139**(9), p. 091016.

[20] Sammons, P. M., Bristow, D. A., and Landers, R. G., 2013, "Height Dependent Laser Metal Deposition Process Modeling," ASME J. Manuf. Sci. Eng., **135**(5), p. 054501.

[21] Nikam, S. H., and Jain, N. K., 2018, "3D-Finite Element Simulation and Image Processing Based Prediction of Width and Height of Single-Layer Deposition by Micro-plasma-Transferred Arc Process," Int. J. Adv. Manuf. Technol., **95**(9–12), pp. 3679–3691.

[22] Donadello, S., Furlan, V., Demir, A. G., and Previtali, B., 2022, "Interplay Between Powder Catchment Efficiency and Layer Height in Self-stabilized Laser Metal Deposition," Opt. Lasers Eng., **149**, p. 106817.

[23] Hofman, J., Pathiraj, B., van Dijk, J., de Lange, D., and Meijer, J., 2012, "A Camera Based Feedback Control Strategy for the Laser Cladding Process," J. Mater. Process. Technol., **212**(11), pp. 2455–2462.

[24] Gibson, B., Bandari, Y., Richardson, B., Henry, W., Vetland, E., Sundermann, T., and Love, L., 2020, "Melt Pool Size Control Through Multiple Closed-Loop Modalities in Laser-Wire Directed Energy Deposition of Ti–6Al–4V," Addit. Manuf., **32**, p. 100993.

[25] Fox, M. D. T., Hand, D. P., Su, D., Jones, J. D. C., Morgan, S. A., McLean, M. A., and Steen, W. M., 1998, "Optical Sensor to Monitor and Control Temperature and Build Height of the Laser Direct-Casting Process," Appl. Opt., **37**(36), pp. 8429–8433.

[26] Toyserkani, E., and Khajepour, A., 2006, "A Mechatronics Approach to Laser Powder Deposition Process," Mechatronics, **16**(10), pp. 631–641.

[27] Song, L., Bagavath-Singh, V., Dutta, B., and Mazumder, J., 2012, "Control of Melt Pool Temperature and Deposition Height During Direct Metal Deposition Process," Int. J. Adv. Manuf. Technol., **58**(1–4), pp. 247–256.

[28] Yeung, H., Yang, Z., and Yan, L., 2020, "A Meltpool Prediction Based Scan Strategy for Powder Bed Fusion Additive Manufacturing," Addit. Manuf., **35**, p. 101383.

[29] Yang, Z., Lu, Y., Yeung, H., and Krishnamurty, S., 2019, "Investigation of Deep Learning for Real-Time Melt Pool Classification in Additive Manufacturing," In 2019 IEEE 15th International Conference on Automation Science and Engineering (CASE), Vancouver, BC, Canada, Aug. 22–26, IEEE, pp. 640–647.

[30] Francis, J., and Bian, L., 2019, "Deep Learning for Distortion Prediction in Laser-Based Additive Manufacturing Using Big Data," Manuf. Lett., **20**, pp. 10–14.

[31] Yang, Z., Lu, Y., Yeung, H., and Krishnamurty, S., 2020, "From Scan Strategy to Melt Pool Prediction: A Neighboring-Effect Modeling Method," ASME J. Comput. Inf. Sci. Eng., **20**(5), p. 051001.

[32] Zhang, Y., Hong, G. S., Ye, D., Zhu, K., and Fuh, J. Y., 2018, "Extraction and Evaluation of Melt Pool, Plume and Spatter Information for Powder-Bed Fusion AM Process Monitoring," Mater. Des., **156**, pp. 458–469.

[33] Jamnikar, N., Liu, S., Brice, C., and Zhang, X., 2021, "Machine Learning Based In Situ Quality Estimation by Molten Pool Condition-Quality Relations Modeling Using Experimental Data," Int. J. Adv. Manuf. Technol., **121**(1), pp. 903–917.

[34] Caiazzo, F., and Caggiano, A., 2018, "Laser Direct Metal Deposition of 2024 Al Alloy: Trace Geometry Prediction Via Machine Learning," Materials, **11**(3), p. 444.

[35] Qi, X., Chen, G., Li, Y., Cheng, X., and Li, C., 2019, "Applying Neural-Network-Based Machine Learning to Additive Manufacturing: Current Applications, Challenges, and Future Perspectives," Engineering, **5**(4), pp. 721–729.

[36] Ocylok, S., Alexeev, E., Mann, S., Weisheit, A., Wissenbach, K., and Kelbassa, I., 2014, "Correlations of Melt Pool Geometry and Process Parameters During Laser Metal Deposition by Coaxial Process Monitoring," Phys. Procedia, **56**, pp. 228–238.

[37] Wang, Z. J., Turko, R., Shaikh, O., Park, H., Das, N., Hohman, F., Kahng, M., and Polo Chau, D. H., 2021, "CNN Explainer: Learning Convolutional Neural Networks With Interactive Visualization," IEEE Trans. Vis. Comput. Graph., **27**(2), pp. 1396–1406.

[38] Chang, C.-C., and Lin, C.-J., 2011, "LIBSVM: A Library for Support Vector Machines," ACM Trans. Intell. Syst. Technol., **2**(3), pp. 1–27.

[39] Panigrahi, S., and Mantri, J. K., 2015, "Epsilon-SVR and Decision Tree for Stock Market Forecasting," In 2015 International Conference on Green Computing and Internet of Things (ICGCIoT), Greater Noida, Delhi, India, Oct. 8–10, pp. 761–766.

[40] Wong, T.-T., and Yeh, P.-Y., 2020, "Reliable Accuracy Estimates From *k*-Fold Cross Validation," IEEE Trans. Knowl. Data Eng., **32**(8), pp. 1586–1594.

[41] Nembrini, S., König, I. R., and Wright, M. N., 2018, "The Revival of the Gini Importance?," Bioinformatics, **34**(21), pp. 3711–3718.

[42] Duval, A., 2019, "Explainable Artificial Intelligence (XAI)," MA4K9 Scholarly Report University of Warwick, pp. 1–53.